



Modifying the photocatalytic property of ZnO-based photoelectrodes by introducing MgFe₂O₄ nanoparticles

Sanchari Banerjee¹, Subhash Padhan², and R. Thangavel^{1,*}

¹Department of Physics, Indian Institute of Technology (Indian School of Mines), Dhanbad, Jharkhand 826004, India

²Department of Chemistry, Indian Institute of Technology (Indian School of Mines), Dhanbad, Jharkhand 826004, India

Received: 29 April 2021

Accepted: 20 October 2021

Published online:

28 October 2021

© The Author(s), under exclusive licence to Springer Science+Business Media, LLC, part of Springer Nature 2021

ABSTRACT

Limited light absorption and acute charge recombination on the surface of ZnO nanostructure-based photoelectrodes are the basic challenges to be grappled with for better photoelectrochemical performance. Here, in this study, we attempted to fabricate a methodical and sturdy nano-heterojunction photoelectrode by anchoring chemically stable spinel ferrite (MgFe₂O₄) nanoparticles (NPs) on ZnO nanorod (NR) arrays. The magnetic ferrites with a low band gap improve the ability of nano-heterojunction photoelectrodes to harvest solar energy in the visible region which further enhances the photocurrent density and photoelectrochemical conversion efficiency (PCE), respectively, when compared to pure ZnO NR. The optimized sample MFZ_3 h exhibited the most intense photocurrent density 0.54 mA/cm² among all the samples. The band alignment at the MgFe₂O₄/ZnO nano-heterojunction enables significant charge transfer and separation properties. The photoelectrode composed of hybrid nanostructure provides long term durability. This work denotes an easy yet fruitful strategy of developing cost-effective earth-abundant magnetite-based heterojunction photoelectrodes that act as an effective photocatalyst for photoelectrochemical water splitting (PEC) application.

1 Introduction

Non-conventional energy resources (Biomass, Solar and Wind energy) etc. has gained considerable importance in the present era, with ever-increasing environmental pollution and depletion of fossil reserves [1]. Successfully establishing a photoelectrochemical cell to produce clean energy via water splitting and dealing with CO₂ emission by utilizing abundant renewable resources (Solar energy) is a

favorable approach to meet the rising energy demand [2]. Photoelectrodes based on semiconductors caught acute attention for photoelectrochemical water splitting (PEC), where electrodes can be designed as anode/cathode depending on their usage for water oxidation or reduction reactions. So far, metal oxide semiconductors (ZnO, Fe₃O₄, BiVO₄, TiO₂) and their composites have been substantially investigated as an efficient photoelectrode for photoelectrochemical performances [3]. Among them, ZnO materialized as

Address correspondence to E-mail: rthangavel@iitism.ac.in

a propitious photoelectrode candidate due to its favorable properties. The conduction and valence band position of ZnO stands out to be appropriate for PEC application. But it carries the disadvantage of being a light absorber only in the UV region due to its large band gap (~ 3.37 eV). Generally, the following properties should be possessed by ideal photoanodes participating in the PEC realm: wide range solar light absorption to generate more number of charge carriers, low recombination rate for an improved electron–hole (e^- -h) pair separation and its enhanced photostability. Hereby, to improve the photoconversion efficiency of ZnO-based photoanodes, different approaches have been strategized [4]. A constructive approach of forming heterostructures allured new scientific minds as in this technique the outer coated material can absorb wide range solar spectrum and generate charge carriers subsequently transferring it to the base material which accordingly suppress recombination rate and facilitates charge separation. Recently, to utilize the wide range solar spectrum for an enhanced photoelectrochemical response spinel ferrites were used conjointly with semiconductors having wide band gap e.g., ZnO. Ferrite nanoparticles grabbed appreciable recognition due to their technological significance and biological application. Their low toxicity, excellent magnetic properties, biocompatibility and multifaceted surface functionalization makes them a potential candidate for environmental applications. It is conventional that magnetite ($MgFe_2O_4$) is a soft magnetic n-type semiconductor and possess a small band gap. With their band gap ranging from 1.9 to 2.5 eV, they have marked their potentiality in photocatalysis. They possess high STH efficiency which indicates their outstanding visible light response, photoelectrochemical stability and suitable band positions for water oxidation/reduction reaction. Additionally, the ferrites composites also facilitate charge separation due to its magnetically induced separable property. Consequently, due to their low band gap it can be effective in absorbing visible light [5, 6]. Zhang et al. synthesized $MgFe_2O_4$ - TiO_2 nanocomposites (NCs) that exhibited enhanced visible light photoelectrochemical response [7]. Yang et al. synthesized 3D macroporous ZnO/ $ZnFe_2O_4$ nanostructures using in-situ thermal solid reactions for remarkable photoelectrochemical water splitting application [8]. Lan et al. reported $ZnFe_2O_4$ / ZnO core–shell heterojunction nanostructure using simple ion etching method

showing enhanced photoelectrochemical performance [9]. Qin et al. reported heterojunction nanostructure consisting of ZnO and $ZnFe_2O_4$ that was synthesized using drop coating technique exhibiting appreciable photoelectrochemical performance under visible light irradiation [10].

In this work, a low-cost hydrothermal approach has been taken to synthesize $MgFe_2O_4$ NPs decorated ZnO NR heterostructure (MFZ). The main motto of designing these composite was to modify the band gap of the material which subsequently facilitate visible light-induced photoelectrochemical activities. Secondly, opting for non-hazardous elements so that additional pollution can be avoided making the overall system environment friendly.

2 Experimental details

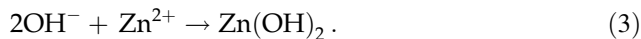
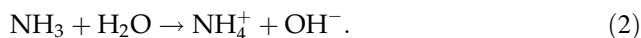
2.1 Synthesis procedure

2.1.1 Preparation of ZnO NRs

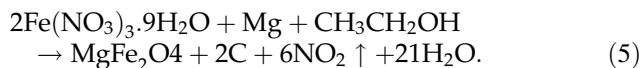
A two-step method was utilized to fabricate ZnO NRs on ITO coated glass substrates with a geometric thickness of 1 cm. Initially, the zinc precursor (Zinc acetate dihydrate) was dissolved in an appropriate amount of solvent 2methoxyethanol (2ME). The solution was stirred vigorously and mono-ethanolamine (MEA) was used as the stabilizer. It was further stirred for a duration of 2 h at 60 °C and aged for 24 h to obtain the ZnO seed solution. The solution was then used for spin coating maintaining rpm of 2500 for 20 s. The extra residuals were evaporated by heating the coated surface in a hot plate at 150 °C for 10 min. To obtain the desired thickness the coating and drying process was repeated four times. The ZnO seed layer was obtained by annealing the acquired thin film in the air furnace at 400 °C. ZnO NR assemblage was then grown via hydrothermal technique. The obtained ZnO seed layer coated ITO substrate was inversely submerged in the growth solution comprising of equimolar solution i.e., 0.5 M Zinc nitrate hexahydrate and 0.5 M hexamethylenetetramine (HMT) at 95 °C for 5 h. The final NR grown film was cleaned using DI water and subsequently oven-dried.

2.1.2 Preparation method of MF NPs and MFZ NCs

The method opted for synthesizing magnetite MgFe_2O_4 (MF) NPs were as follows: 0.17 M $\text{Fe}(\text{NO}_3)_3 \cdot 9\text{H}_2\text{O}$ and 0.03 M metallic Mg powders were used as the initial precursor. Firstly, an aqueous solution of $\text{Fe}(\text{NO}_3)_3$ and Mg powder was prepared with ethanol. After vigorous stirring for 2 h the synthesized product was autoclaved at 180 °C for 12 h. After cooling to room temperature the obtained dark precipitate was dispersed in 10 ml cyclohexane and subsequently centrifuged at 8000 rpm to remove the minute impurities that might be present. The transparent red colloidal precipitate obtained was re-dispersed in cyclohexane. To prepare MFZ nanoarrays, the ZnO NR was submerged upside down in the re-dispersed magnetite solution maintaining different deposition times (1 h, 3 h, 5 h) to obtain the required thickness of the different layers. The substrates were cleaned with DI water and then annealed at 500 °C for 1 h. The reaction mechanism of MF/ZnO heterojunction is illustrated with the following reactions. ZnO seed layers were obtained via sol-gel synthesis and subsequent annealing in air. Consequently, ZnO NRs were grown by placing the seeded ZnO substrate in the growth solution.



The Iron source ferric nitrate is ethanol friendly. With the assistance of ferric nitrate, Mg powder can disperse well in absolute ethanol due to the interaction taking place between Fe^{3+} and electrons on the metallic Mg surface.



2.2 Characterization

The overall structural and morphological properties of annealed pure ZnO and MF NPs decorated ZnO NR were analyzed by Grazing Incidence X-ray Diffraction (GIXRD, Rigaku smart lab XRD) with $\text{Cu K}\alpha$ monochromator radiation source with ($\lambda = 0.154 \text{ \AA}$) and Field Emission Scanning Electron Microscope (FESEM, Carl Zeiss Supra 55). The

analysis of atomic composition by elemental mapping of the NR film was done by EDX spectroscopy. The recorded UV-Vis absorption spectra in the wavelength 300–700 nm were obtained via Agilent Cary 5000 UV-Vis-NIR double beam spectrophotometer.

2.3 Photoelectrochemical measurements

Visible-light-induced photoelectrochemical measurements of pure ZnO and MF NPs decorated ZnO NR were executed in an encompassed electrochemical workstation (CHI 660C, CH instrument) with a cell comprising of three electrodes with a visible light source (Intensity: 20 mW/cm^2 , $\lambda > 420 \text{ nm}$). The prepared pure and decorated heterostructure samples grown on ITO/glass substrate were used as the working electrode, a saturated Ag/AgCl as the reference and Pt wire served as counter electrode, respectively, the electrolyte used was 0.1 M KOH aqueous solution. The photocurrent density measurements were carried out in dark and light conditions within a potential of 0 to 1.2 V vs Ag/AgCl.

3 Results and discussion

3.1 Structural properties

GIXRD is generally used to analyze the crystalline structure of thin films and coatings. Figure 1 shows the GIXRD pattern of pure ZnO nanorod (NR) and MF/ZnO nanocomposite (NC). XRD pattern of the

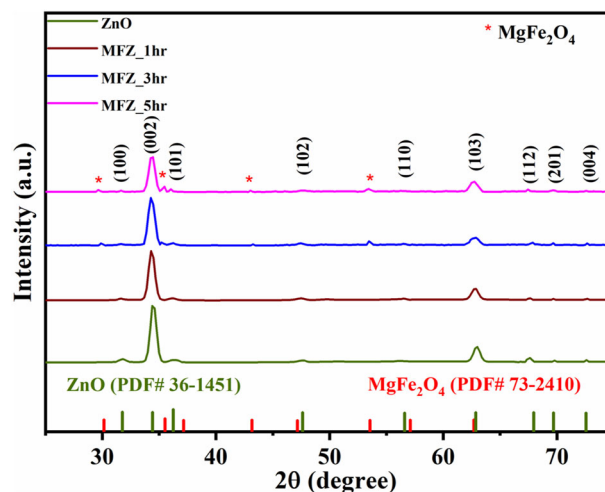


Fig. 1 XRD patterns of (a) bare ZnO NR (b) MFZ_1 h (c) MFZ_3 h (d) MFZ_5 h

synthesized pure ZnO were well-matched with JCPDS card no: 36-1451. The characteristics peaks showed by this pattern were positioned at 31.5°, 34.2°, 36.3°, 47.6°, 56.6°, 62.7°, 67.6°, 69.3°, 72.5° attributed to the planes (100), (002), (101), (102), (110), (103), (112), (201) and (004). This stipulates the hexagonal wurtzite nature of bare ZnO, its high intense peak along (002) plane shows the preferred orientation of the ZnO NRs along the c-axis [11, 12]. After coating ZnO base material with magnetite (MF) some of the corresponding diffraction peaks associated were observed and were positioned at 30.3°, 35.5°, 43.2° and 53.3° analogous to (220), (311), (400), (422) plane. They were well-matched with the JCPDS card no: 73-2410. The peaks obtained after coating MF were less intense and less prominent in comparison to ZnO NR which might be due to their low crystallinity. Moreover, the characteristic peaks corresponding to MF were perceptible only for those samples that were dipped for a longer duration i.e., MFZ_3 h and MFZ_5 h. As the ZnO NR is decorated with MF nanoparticles the dominant peak of ZnO corresponding to (002) plane shifts towards lower theta angle this confirms that Zn²⁺ ion is not substituted by Fe³⁺ in the ZnO host lattice. As, if it had happened then the main crystal plane (002) would have shifted towards a higher angle because the ionic radius of Fe³⁺ ion is lesser than that of Zn²⁺ ion. The crystal size of MFZ NCs is smaller than that of pure ZnO as calculated by the Scherrer formula. The structural parameters including lattice parameters 'a', 'c' for ZnO; 'a' for MgFe₂O₄ and unit cell volume of the nanocomposite as listed in Table 1 using the following equations.

$$D = \frac{K\lambda}{\beta_{hkl} \cos \theta} \quad (6)$$

$$\frac{1}{d^2} = \frac{4}{3} \left(\frac{h^2 + hk + k^2}{a^2} \right) + \frac{l^2}{c^2} \quad (7)$$

$$\frac{1}{d^2} = \left(\frac{h^2 + k^2 + l^2}{a^2} \right) \quad (8)$$

$$V = 0.866a^2c \quad (9)$$

$$V = a^3 \quad (10)$$

where D is the crystallite size, K is a numerical shape factor related to crystallite-shape information. Since, we do not know the exact value of the K for present system, all crystallite size calculations were estimated considering $K = 0.9$, λ and β are the wavelength

Table 1 The calculated structural parameters of all the synthesized samples

Sample	Pure ZnO	MFZ_1 h	MFZ_3 h	MFZ_5 h
ZnO, a (Å)	3.262	3.257	3.260	3.259
c (Å)	5.209	5.225	5.229	5.223
V (Å)	48.01	47.99	48.12	48.04
MgF, a (Å)			8.422	8.385
V (Å)			595.5	589.5
D (nm)	40	20	16	11

Value of lattice constants and unit cell volume obtained from the XRD pattern

(1.54 Å) and peak width half maxima, respectively [13]. The other parameters d and hkl are the interplanar spacing and miller indices, respectively; a , c is the lattice parameter of hexagonal structure similarly a is the lattice constant of cubic MgFe₂O₄.

3.2 Morphological properties

Figure 2 shows FESEM images of the synthesized pure ZnO NR and MFZ NC grown on ITO coated glass substrate. The ZnO NR exhibited hexagonal structures that were vertically aligned. From Fig. 2a it can be seen that the NRs possess a smooth surface with nearly uniform size. The diameter of the synthesized samples was measured via ImageJ software and it lies in the range of 60 to 120 nm. The morphology of ZnO NRs changed with the decoration of MgF NPs on it. The MgF NPs were physically absorbed and it entirely covered the ZnO NRs [14]. Compared to pure ZnO the surface of MFZ NCs became rough thereby increasing the surface area and providing more active sites for the photoelectrochemical water oxidation reaction. As the dipping duration increased, the MF NPs fully covered the ZnO NRs. It not only lessened the gap between the NRs but also slightly changed their hexagonal structure. The underlying reason behind these was the spherical NPs that coated the ZnO NRs, it engulfed the hexagonal edge surface of the NRs. It embodied a layer of itself on the pure ZnO NRs and subsequently, the diameter of MgF NPs coated ZnO NRs increased. Elemental distribution of MF/ZnO NCs was probed via EDX elemental mapping [15]. The mapping images exhibited uniform distribution of Zn, O, Mg and Fe which substantiates the

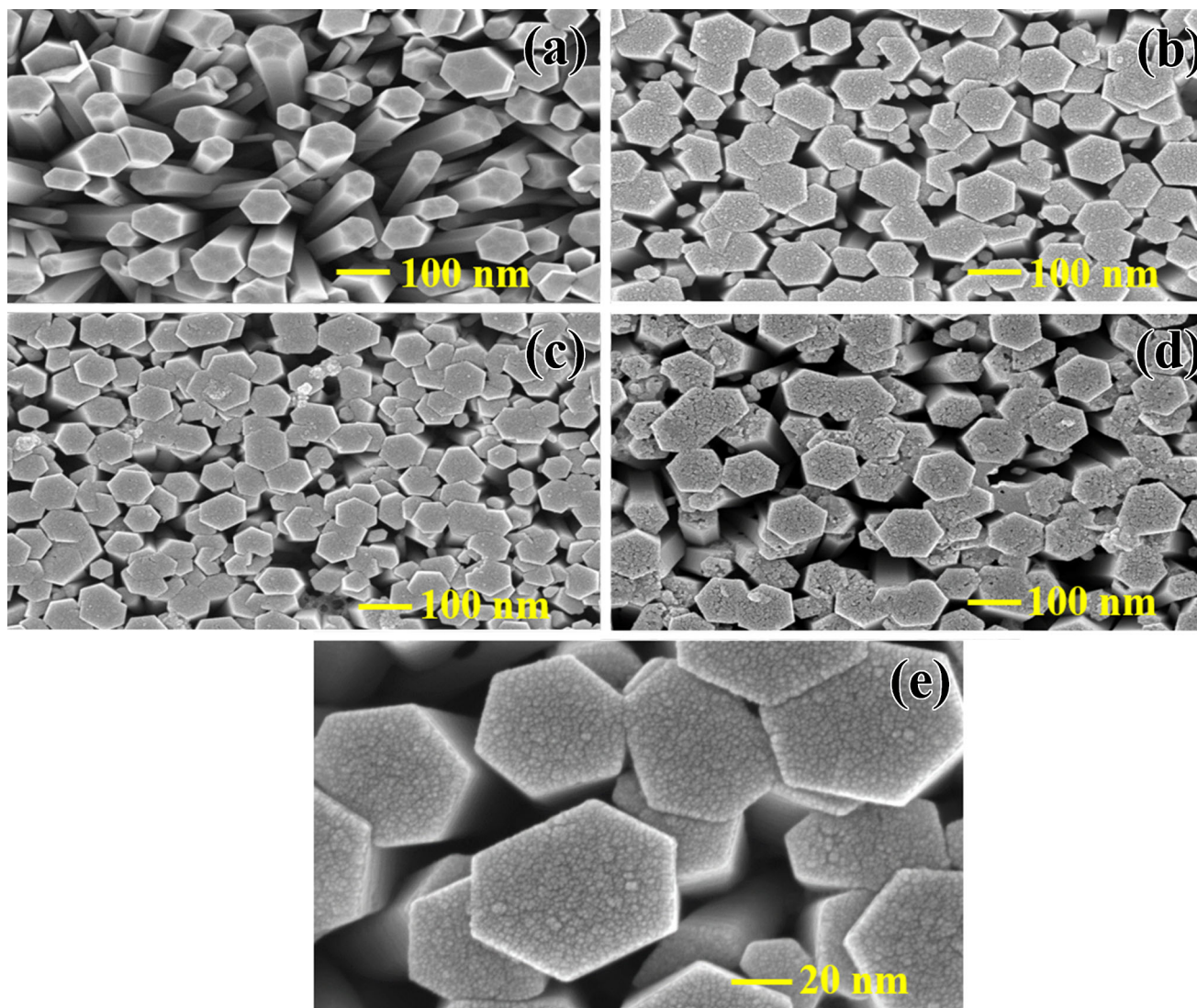


Fig. 2 FESEM images of **a** Pure ZnO, **b** MFZ_1 h, **c** MFZ_3 h, **d** MFZ_5 h, and **e** MFZ_3 h (magnification: 20 nm)

coexistence of MgF and ZnO counterparts in MFZ NCs as shown in Fig. 3.

3.3 X-ray photoelectron spectroscopy

Figure 4 shows the XPS spectroscopic result of MFZ_3 h. Elemental-specific scans with fitted peak positions, are shown. The peaks positioned at 1021 eV and 1045 eV can be assigned to Zn 2p_{3/2} and Zn 2p_{1/2}. Fe 2p peaks at 710.8 eV, 712 eV, 724.38 eV with a satellite peak at 718.32 eV and 732.26 eV corresponds to Fe³⁺ oxidation state. From O 1s scan, two distinct peaks are obtained at 529.21 eV depicting the presence of lattice oxygen in metal–oxygen bond while the second peak at 531.29 eV represents the presence of oxygen vacancies in the sample. The

Mg 2s scan data is deconvoluted into two peaks that originates due to MgO [16, 17].

3.4 Optical properties

To modify the photocatalytic activity of the photocatalysts either doping or coupling with transition metals has been done by many researchers. Doping process helps in reducing band gap which further prevents recombination of e⁻-h pair ameliorating photocatalytic activities. Such doped or coupled ZnO with a reduced band gap will be able to respond under both UV and visible irradiation [18]. Due to the narrow band gap MF NPs absorbs visible light. On the other hand, due to the wide band gap of ZnO, it strongly absorbs UV light and feebly absorbs visible

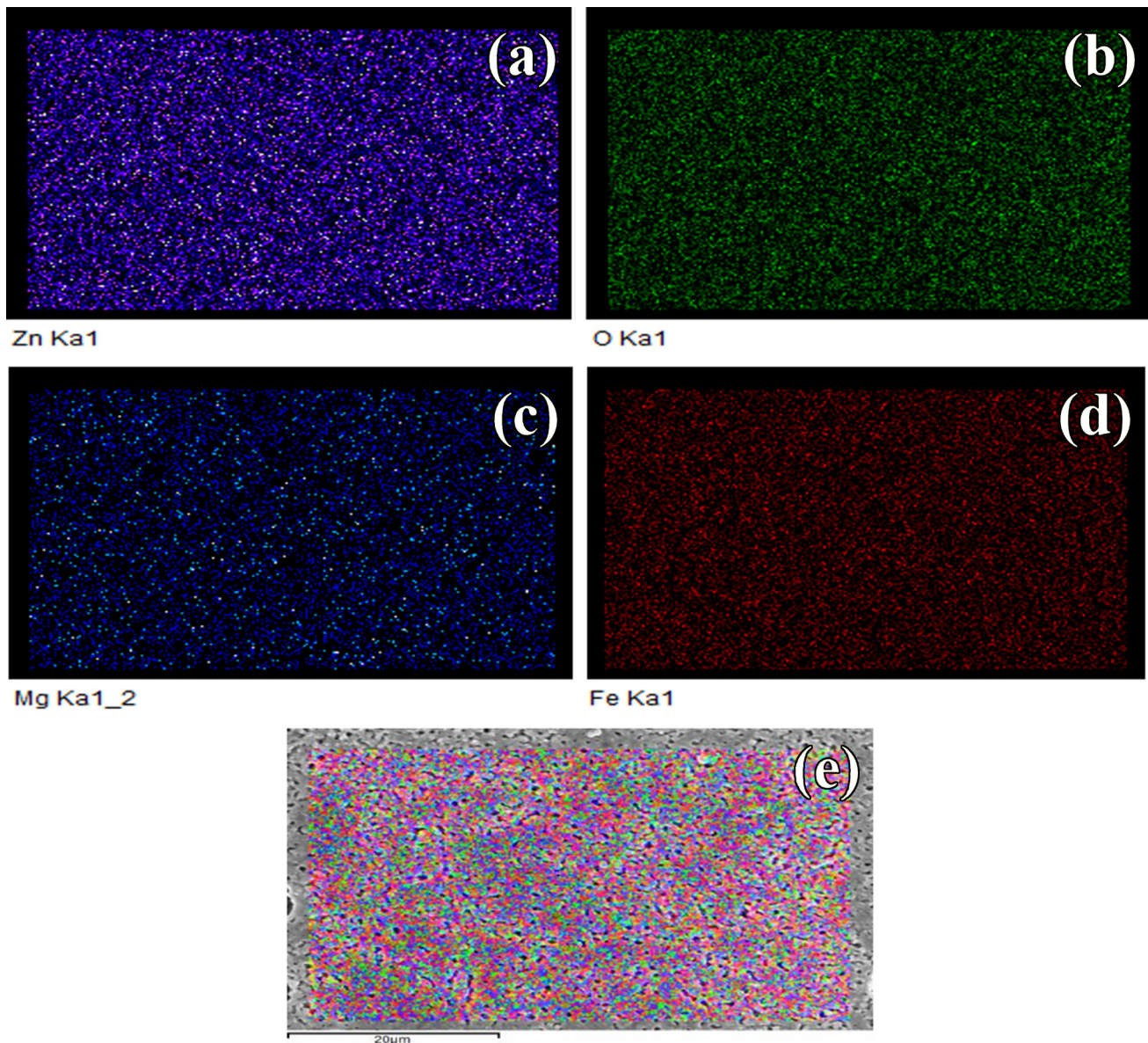


Fig. 3 EDX mapping of MFZ_3 h with different coexisting elements (Zn, O, Mg, Fe)

light. Thus, integrating both these materials enhances the absorbance of visible light. As coating MF layer has the ability to absorb more visible photons Fig. 5 shows the optical absorption spectra of the synthesized films. It can be observed that the absorption edge of pure ZnO NRs and MgFe₂O₄ NPs-based thin films were positioned at about 390 nm and 530 nm, respectively [19]. Compared to pure ZnO NR the decorated samples (MFZ_1 h, MFZ_3 h and MFZ_5 h) have shown a redshift. The band gap obtained from the Tauc plot of pure ZnO NR and MF NPs were measured from the following equation and listed in Table 2.

$$(\alpha h\nu)^n = A(h\nu - E_g) \quad (11)$$

The conduction and the valence band potential of the samples can be evaluated with the following equations.

$$E_{CB} = \chi - E^e - 0.5E_g \quad (12)$$

$$E_{VB} = E_{CB} + E_g \quad (13)$$

where χ is the absolute electronegativity, E_{CB} and E_{VB} represent the conduction and valence band potentials. E^e is the free electron energy on a hydrogen scale (4.5 eV) [20]. The E_{CB} and E_{VB} values of pure ZnO NR and MF NPs are listed in Table. 2. Our

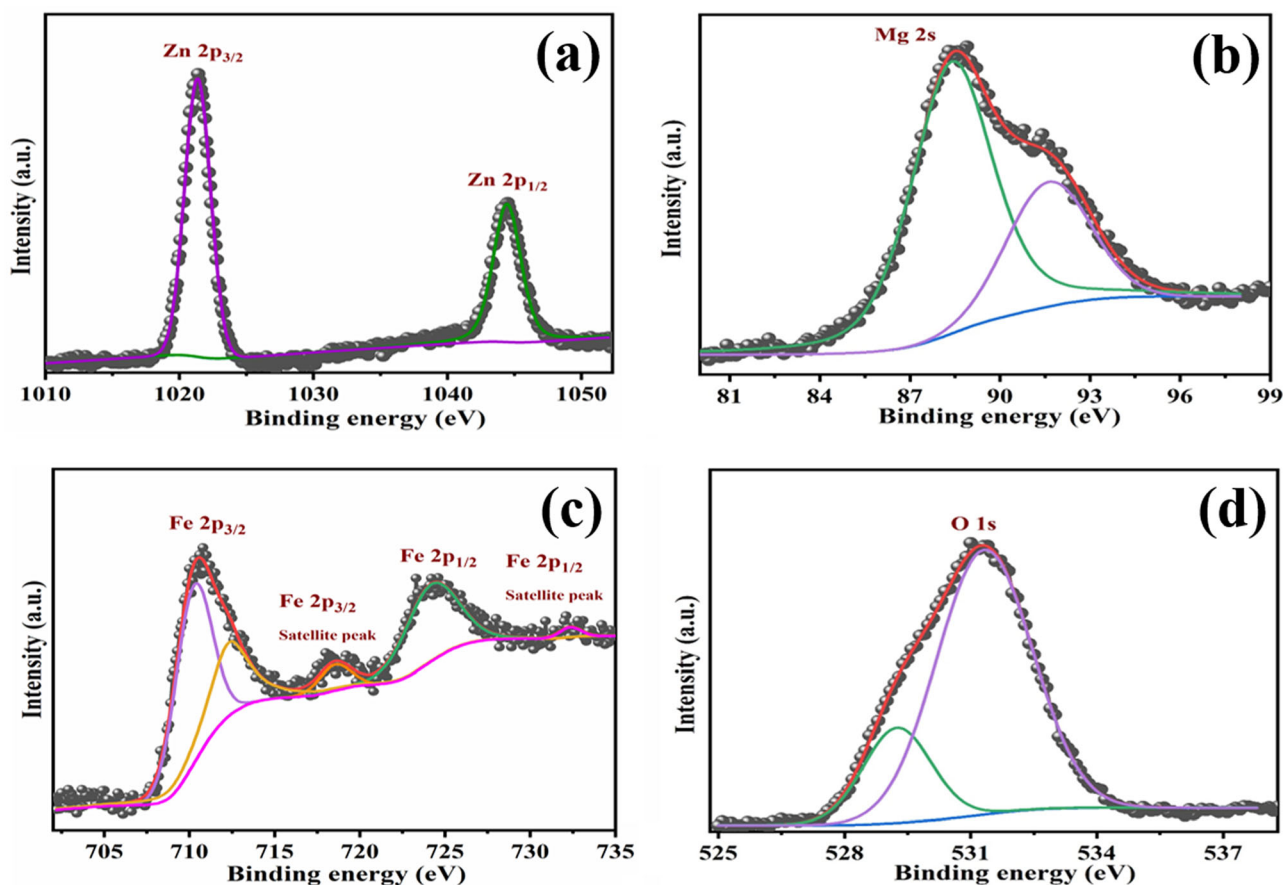


Fig. 4 XPS element-specific scan of different coexisting elements (Zn, Mg, Fe, O)

previously reported work has mentioned absolute electronegativity value of pure ZnO [21].

3.5 Photoelectrochemical tests

The conditions needed for an effective photo-induced water oxidation application are photogeneration of e^- - h pair, low rate of charge recombination and effective charge separation by the photoelectrodes. The commencement of redox reaction can arise due to the depletion layer in the electrode/electrolyte interface [22]. To study the photoelectrochemical performance of the synthesized samples, pure ZnO and MF NPs decorated ZnO NRs; Platinum wire and Ag/AgCl were taken as the working, counter and reference electrode, respectively, in a photoelectrochemical chamber under light illumination (20 mW/cm², wavelength > 420 nm), along with 0.1 M KOH as the active electrolyte throughout the analysis. The most common electrochemical approach i.e., Linear Sweep Voltammetry (LSV) is used to investigate charge carrier properties of the electrode/electrolyte

interface [23]. Figure 6a manifested the LSV (current–voltage) curve obtained for pure ZnO NR and MF NPs decorated ZnO NRs simultaneously in the presence and absence of light. The photocurrent density of pure ZnO NR under dark conditions is approximately 0.016 mA/cm² subsequently the same shows a slight increment under visible light illumination but the magnitude is almost negligible compared to the photocurrent density obtained with the deposition of MF. All the MF NPs decorated ZnO heterostructures exhibited a noticeable response in presence of light. The results are consistent with the previously mentioned UV–Vis spectral analysis of the corresponding samples shown in Fig. 5 confirming the enhancement of photocurrent density is due to the band gap transition of MF. MFZ_3 h showed the highest photocurrent density under light illumination (0.54 mA/cm²) followed by MFZ_1 h (0.212 mA/cm²) and MFZ_5 h (0.110 mA/cm²). Additionally, a negative shift of the onset potential of all the decorated samples compared to pure ZnO can be

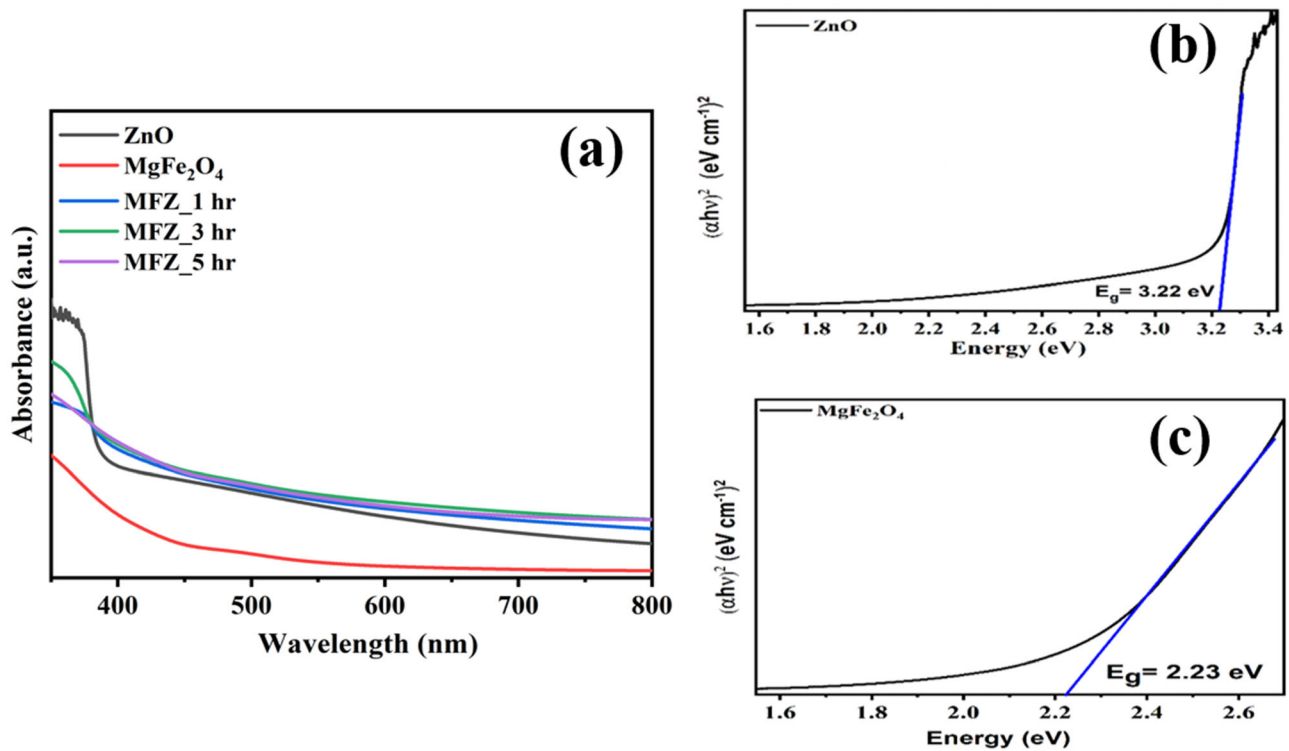


Fig. 5 a Absorbance spectra of the synthesized sample. b Tauc plot of pure ZnO NR. c Tauc plot of MgF NPs

Table 2 The estimated values of the optical band gap, absolute electronegativities, conduction and valence

Sample	E_g (eV)	Absolute electronegativity (χ)	E_{CB} (eV)	E_{VB} (eV)
ZnO	3.22	5.950	- 0.161	3.059
MgFe ₂ O ₄	2.23	4.899	- 0.701	1.499

observed which indicates a reduction in charge recombination rate in the heterojunction. All the synthesized samples experienced a chronoamperometric test to get an insight into the interfacial charge transfer rate, charge carrier separation and the response of photocurrent under discontinuous visible light illumination [24, 25]. Figure 6b showed the calculated photoconversion efficiency (PCE %) of the synthesized samples vs applied voltage. The PCEs (%) of pure ZnO, MFZ_1 h, MFZ_3 h, MFZ_5 h were measured to be 0.003%, 0.09%, 0.184%, 0.02%, respectively. The photocurrent response of all the samples at zero bias voltage vs Ag/AgCl is shown in Fig. 6c. A transient photocurrent materializes as soon as the light is switched on which indicates the presence of surface states in MF. The deep energy level capture caused by the existence of surface states thus leads to the recombination of charged pairs and consequently, transient photocurrent appears. The similar nature of *i-t* curves was discerned for all the

samples upon light irradiation. The photocurrent density rose flashily and remained constant upon illumination and then abruptly decreased to a steady state as the light is chopped off. Despite the underlying similarities, differences in photocurrent response were observed. Enhanced photoresponse of all the MF NPs decorated ZnO heterostructures were seen compared to the pure state. Among all, MFZ_3 h exhibited the highest photoresponse indicating its better charge separation property and low recombination rate [26]. A stability test was also carried out for a continuous duration of 3 h in absence of bias voltage under light illumination [27]. Initially, the photocurrent response showed a sharp rise but gradually decreased and came to a stable state within a short span as shown in Fig. 6d.

To compare the photoelectrocatalytic performance of MF/ZnO heterojunction structure against their pristine state it is important to find out the specific activity of the photocatalytic material via

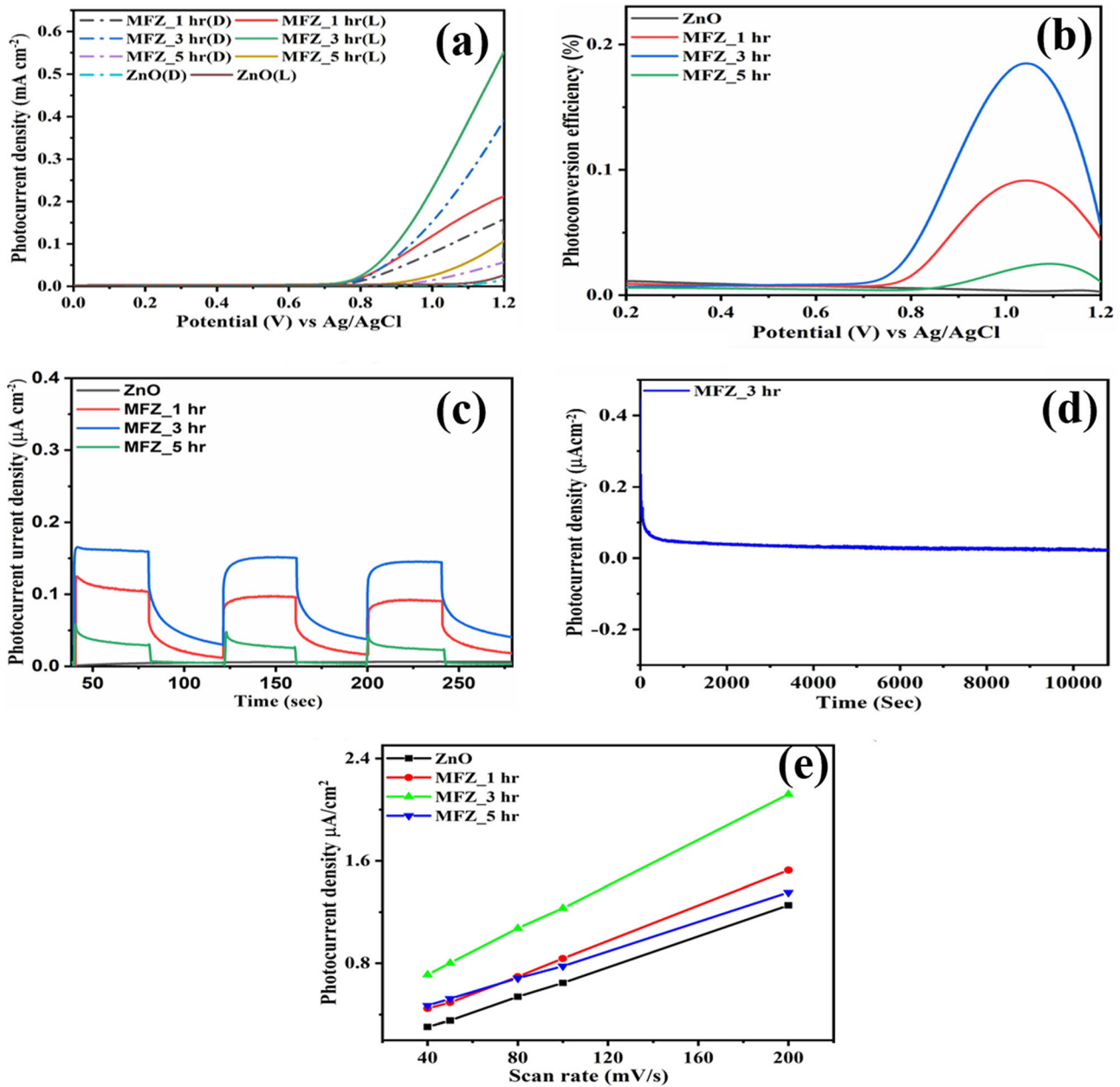


Fig. 6 **a** LSV polarization curves of synthesized samples at 10 mV/s. **b** Photocurrent efficiency of the samples under visible light illumination. **c** i-t curves of all the synthesized samples.

d The chronoamperometric stability test. **e** Photocurrent density vs Scan rate plot of the synthesized samples

electrochemically active surface area (ECSA). ECSA was evaluated from the electrochemical double-layer capacitance as reported in previous literature. The double-layer charging current (i_{dl}) arising in the non-Faradaic region was measured using cyclic voltammograms with different scan rates [28]. The average of the cathodic and anodic i_{dl} slopes was used to determine the electrochemical double-layer capacitance (C_{dl}). C_{dl} is directly proportional to ECSA

which indicates that higher C_{dl} represents larger ECSA as shown in Fig. 6e.

$$i_{dl} = C_{dl} \times v \tag{14}$$

$$ECSA = C_{dl}/C_s \tag{15}$$

where V is the voltage and C_s is the specific capacitance (0.040 mF/cm^2).

Moreover, the electrochemical impedance spectroscopy (EIS) analysis of all the synthesized samples

was carried out under visible light irradiation. It enables us to get a better understanding of the property of charge transfer taking place within the photoelectrode-electrolyte interface [29, 30]. The Nyquist plots of the bare and decorated ZnO NRs shown in Fig. 7a were plotted at a bias voltage of 0 V vs Ag/AgCl at a frequency ranging from 0.01 Hz to 100 kHz. The diameter of the arc represented the charge transfer activity within the semiconductor/electrolyte interface. The reduced arc diameter of the Nyquist plot indicates proficiency in charge transfer activity and recombination rate [31]. From Fig. 7a, it can be observed that compared to pure ZnO, the MF decorated ZnO NCs shows better charge transfer property and low recombination rate. The introduction of MF NPs improves the charge transfer property which might be the effect of band alignment formation between the constructed heterojunction. As the hybrid composite gets illuminated the photo-excited charge pairs near the ZnO-MF interface rapidly separate and flows towards the opposite direction that furnishes low charge transfer resistance and magnified photocurrent density. But ZnO NRs decorated with more MF NPs as in the case of MFZ_5 h had to suffer charge recombination that minimizes the interfacial charge transfer.

The derivation of the capacitance of ZnO NR and MFZ NCs-based electrodes in absence of light at the interfacial surface were depicted via Mott-Schottky (M-S) plot. All the synthesized samples in the M-S plot exhibited positive value as shown in Fig. 7b indicating the n-type nature of the semiconductors

where electrons act as majority carriers [32]. The MS equation connects the capacitance of the hybrid composite to the carrier concentration represented by N_d along with some other constants and parameters such as electronic charge (e), permittivity of vacuum (ϵ_0), relative permittivity of the semiconductors (ϵ), Boltzmann constant (k_B), temperature (T) and flat band potential (V_{fb}).

$$\frac{1}{C^2} = \frac{2}{e\epsilon\epsilon_0N_d} \left(V - V_{fb} - \frac{k_B T}{e} \right) \quad (16)$$

The extrapolation of the x-intercept of the linear region enabled the measurement of V_{fb} . MFZ_1 h and MFZ_3 h showed smaller slopes compared to pure ZnO NR and MFZ_5 hr stipulating higher carrier densities of the former. The V_{fb} value of pure ZnO, MFZ_1 h, MFZ_3 h and MFZ_5 h were measured and listed in Table 3. MFZ_3 h exhibited the highest negative shift in its V_{fb} value among all the samples indicating its highest charge carrier concentration. Figure 8 shows the related energy diagram of MF/

Table 3 The estimated flat band potential (V_{fb}), carrier density (N_d) values are mentioned

Sample	V_{fb} (V)	N_d (cm ³)
ZnO	− 0.241	2.1×10^{20}
MFZ_1 h	− 0.422	3.6×10^{21}
MFZ_3 h	− 0.448	6.5×10^{21}
MFZ_5 h	− 0.235	1.8×10^{20}

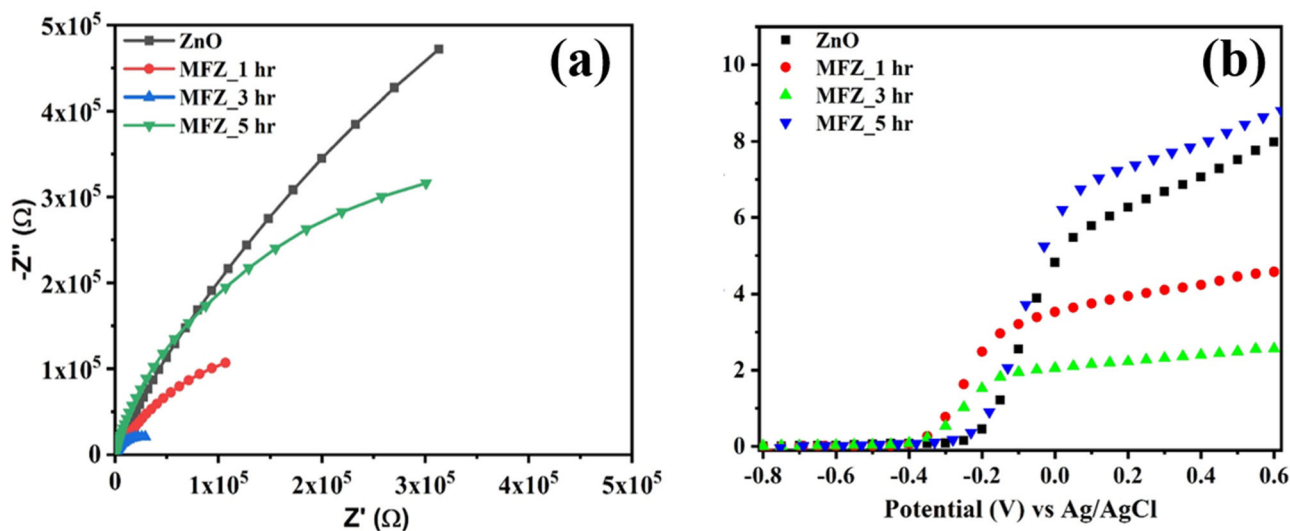
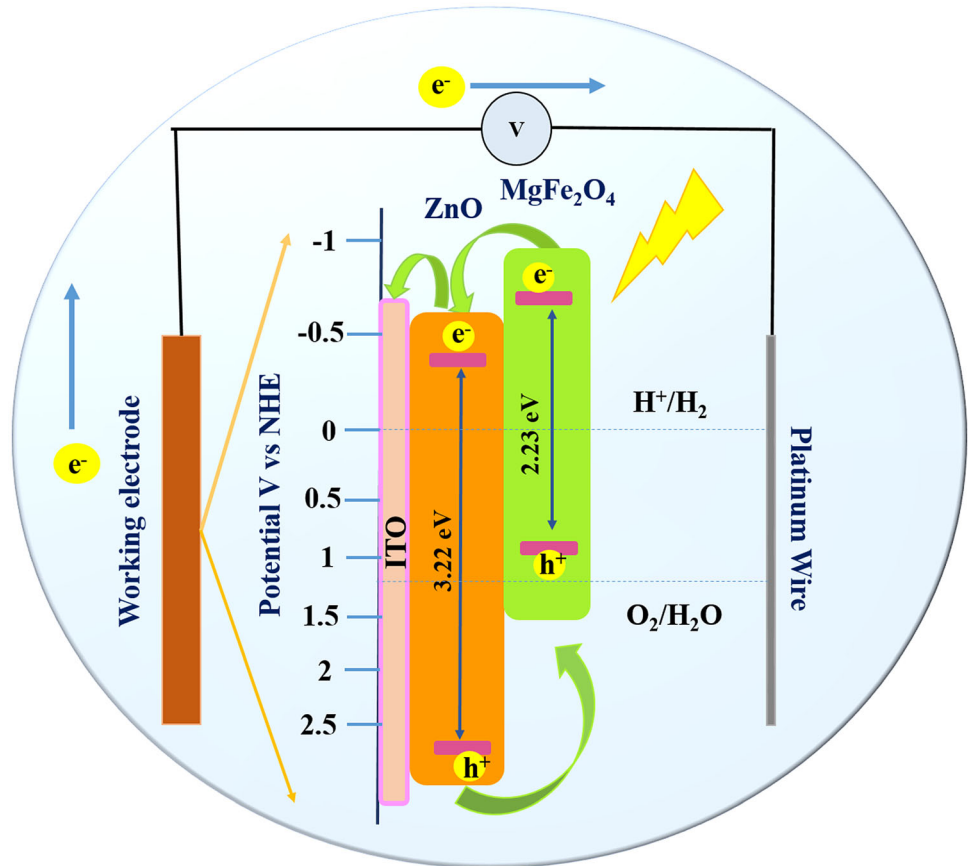


Fig. 7 a EIS Nyquist plot of all the samples under light irradiation. b Mott-Schottky graph of the samples in dark condition

Fig. 8 Schematic representation of the MF/ZnO heterojunction structure



ZnO. The Fermi levels of ZnO and MF at equilibrium will be precisely aligned with the electrolyte solution. The conduction band (CB) and valence band (VB) edges of MF are more negative than those of ZnO which demonstrates a stepwise arrangement of the energy bands in MF/ZnO photoelectrode and allows a well-ordered transfer of photoexcited electrons. Under visible light irradiation, the photoexcited and photogenerated electrons are successfully conveyed from the CB of MF to that of ZnO and subsequently to ITO contact because of the prevailing potential difference. Accordingly, efficient separation of electrons and holes can be acquired where the photogenerated holes present in the VB of ZnO migrate towards the VB of MF averting the assemblage of photogenerated holes at the surface of ZnO and thus shielding the surface from photocorrosion. The photoexcited electrons pave their way towards the cathode for H_2 generation in a PEC cell and conversely, the holes will be swallowed for the water oxidation at the MgFe_2O_4 -electrolyte interface [8, 9].

4 Conclusion

Vertically aligned one dimensional ZnO NRs were synthesized successfully followed by decorating MgFe_2O_4 NPs on ZnO NRs using the hydrothermal technique. With the formation of these NCs, photoactive response under visible light illumination was obtained. MF/ZnO shows an excellent optical response with a broadened light absorption range as confirmed by the UV-Vis study. The low recombination rate and improved interfacial charge transfer property made MF/ZnO heterostructure superior in comparison to bare ZnO NR with photocurrent density.

Acknowledgements

The authors are grateful to IIT(ISM) Dhanbad for providing Research fellowship and Central Research Facilities (CRF). The authors would also like to thank SRM University for providing XRD facility.

Declarations

Conflict of interest The authors declare that they have no known competing financial interests or personal relationships that could have appeared to influence the work.

References

- N.U. Ain, W. Shaheen, B. Bashir, N.M. Abdelsalem, M.F. Warsi, M.A. Khan, M. Shahid, *Ceram. Int.* **42**, 12401–12408 (2016)
- M. Shahid, L. Jingling, Z. Ali, I. Shakir, M.F. Warsi, R. Parveen, M. Nadeem, *Mater. Chem. Phys.* **139**, 566–571 (2013)
- Y. Shen, Y. Wu, X. Li, Q. Zhao, Y. Hou, *Mater. Lett.* **96**, 85–88 (2013)
- J. Jia, X. Du, Q. Zhang, E. Liu, J. Fan, *Appl. Surf. Sci.* **492**, 527–539 (2019)
- M.R. Garcia, M.M. Barba, L. Gutierrez, E.L. Velasco, *J. Nanopart. Res.*, **21** (2019)
- G.M. Kumar, H.D. Cho, D.J. Lee, J.R. Kumar, C. Siva, P. Ilanchezhyan, D.Y. Kim, T.W. Kang, *Chemosphere* **283**, 131134 (2021)
- L. Zhang, Y. He, Y. Wu, T. Wu, *Mater. Sci. Eng. B* **176**, 1497–1504 (2011)
- T. Yang, J. Xue, H. Tan, A. Xie, S. Li, W. Yan, Y. Shen, *J. Mater. Chem. A* **6**, 1210–1218 (2018)
- Y. Lan, Z. Liu, Z. Guo, X. Li, L. Zhao, L. Zhan, M. Zhang, *Dalton Trans.* **47**, 12181–12187 (2018)
- D.D. Qin, C.L. Tao, *RSC Adv.* **4**, 16968 (2014)
- N.R. Su, P. Lv, M. Li, X. Zhang, M. Li, J. Niu, *Mater. Lett.* **122**, 201–204 (2014)
- M. Chakraborty, D. Roy, A. Sharma, R. Thangavel, *Sol. Energy Mater. Sol. Cells* **200**, 109975 (2019)
- X. Lu, X.E. Cao, Y. Liu, X. Li, M. Wang, M. Li, *Int. J. Hydrog. Energy* **43**, 21365–21373 (2018)
- S.S. Kurvanov, S.Z. Urolov, Z.S. Shyamardanov, *Opt. Spectrosc.* **124**, 198 (2018)
- S. Suhaimi, S. Sakrani, T. Dorji, A.K. Ismail, *Nanoscale Res. Lett.* **9**, 256 (2014)
- S. Maitra, R. Mitra, T.K. Nath, *Curr. Appl. Phys.* **27**, 73–88 (2021)
- A.A. Tahir, K.G.U. Wijayantha, *J. Photochem. Photobiol. A: Chem.* **216**, 119–125 (2010)
- J.T. Adeleke, T. Theivasanti, M. Thirupathi, M. Swaminathan, T. Akomolafe, A.B. Alabi, *Appl. Surf. Sci.* **455**, 195–200 (2018)
- A. Gadallah, M.M.E. Nahass, *Adv. Condens. Matter. Phys.* **2013**, 1 (2013)
- F. Khurshid, M. Jeyavelan, M.S.L. Hudson, S. Nagarajan, *R. Soc. Open. Sci.* **6**, 181764 (2019)
- S. Banerjee, S. Padhan, R. Thangavel, *J. Mater. Sci. Mater. Electron* (2021). <https://doi.org/10.1007/s10854-021-07091-y>
- Y. Zu, Y. Zhao, K. Xu, Y. Tong, F. Zhao, *Ceram. Int.* **42**, 18844–18850 (2016)
- J. Chandradass, H. Kim, F.W.Y. Momade, *J. Sol-Gel Technol.* **65**, 189–194 (2013)
- M. Shahid, L. Jingling, Z. Ali, I. Shakir, M.F. Warsi, R. Parveen, M. Nadeem, *Mater. Chem. Phys.* **139**, 566–571 (2013)
- J. Fu, J. Zhang, C. Zhao, Y. Peng, X. Li, Y. He, Z. Zhang, X. Pan, N.J. Mellors, E. Xie, *J. Alloys Compd.* **577**, 97–102 (2013)
- S. Maensiri, M. Sangmanee, A. Weingmoon, *Nanoscale. Res. Lett.* **4**, 221–228 (2009)
- X. Yuan, H. Wang, Y. Wu, X. Chen, G. Zeng, L. Leng, C. Zhang, *Catal. Commun.* **61**, 66–68 (2015)
- X. Cao, E. Johnson, M. Nath, *J. Mater. Chem. A* **7**, 9877–9889 (2019)
- H.G. Kim, P.H. Borse, J.S. Jang, E.D. Jeong, O.S. Jung, Y.J. Suh, J.S. Lee, *Chem. Commun.* (2009). <https://doi.org/10.1039/b911805e>
- M. Li, H.Y. Bai, Z.L. Da, X. Yan, C. Chen, J.H. Jiang, W.Q. Fan, W.D. Shi, *Cryst. Res. Technol.* **50**, 244–249 (2015)
- H. Huang, X. Hou, J. Xiao, L. Zhao, Q. Huang, H. Chen, *Catal. Today* **330**, 189–194 (2019)
- T.F. Hou, M.A. Johar, R. Bopella, M.A. Hassan, S.J. Patil, S.W. Ryu, D.W. Lee, *J. Energy Chem.* **49**, 262–274 (2020)

Publisher's Note Springer Nature remains neutral with regard to jurisdictional claims in published maps and institutional affiliations.